THE JOURNAL OF PHYSICAL CHEMISTRY C

Article

pubs.acs.org/JPCC

Two-Dimensional Porous Electrode Model for Capacitive Deionization

Ali Hemmatifar,[†] Michael Stadermann,[‡] and Juan G. Santiago*[,†]

[†]Department of Mechanical Engineering, Stanford University, Stanford, California 94305, United States

[‡]Lawrence Livermore National Laboratory, 7000 East Avenue, Livermore, California, United States

Supporting Information

ABSTRACT: Ion transport in porous conductive materials is of great importance in a variety of electrochemical systems including batteries and supercapacitors. We here analyze the coupling of flow and charge transport and charge capacitance in capacitive deionization (CDI). In CDI, a pair of porous carbon electrodes is employed to electrostatically retain and remove ionic species from aqueous solutions. We here develop and solve a novel unsteady two-dimensional model for capturing the ion adsorption/desorption dynamics in a flow-between CDI system. We use this model to study the complex, nonlinear coupling between electromigration, diffusion, and advection of ions. We also fabricated a laboratory-scale CDI cell which we use to measure the near-equilibrium, cumulative adsorbed salt, and electric charge as a function of applied external voltage. We use these integral measures to validate and calibrate this model. We further present a detailed computational study of the spatiotemporal adsorption/desorption dynamics under constant voltage and constant flow conditions. We show results for low (20 mM KCl) and relatively high (200 mM KCl) inlet ion concentrations and identify effects of ion starvation on desalination. We show that in both cases electromigrative transport eventually becomes negligible and diffusive ion transport reduces the desalination rate.

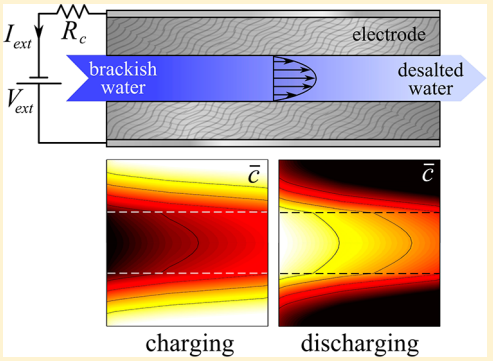

1. INTRODUCTION

Characterizing ionic transport in porous electrodes has been the subject of many research efforts in diverse applications including capacitive water desalination,[1−17] microbial fuel cells,[18,19] energy storage in supercapacitors and batteries,[20−22] and energy recovery via salinity gradients.[23−25] Capacitive desalination, also known as capacitive deionization (CDI), is a relatively new technology that leverages porous electrodes for electrostatic ion adsorption and has potential as an energy-efficient and cost-effective method of the desalination of water with a low to moderate salt content.[26−28] The active component of CDI is a pair of engineered porous carbon electrodes. Upon application of ∼1 V across these electrodes (the charging process), salt ions are removed from feedwater and held electrostatically within electric double layers (EDLs) inside pores. A CDI cell is then regenerated by removing or reversing the voltage (the discharging process), wherein ideally in the absence of Faradaic reactions all of the capacitive charge can be recovered.[29,30] Salt ions are spontaneously released from pores and form brine solution.

CDI cells can be categorized into two groups based on their flow structure: flow through and flow between.[26] In flow-through CDI (ftCDI) cells, the water stream flows directly through the electrode pores, enabling faster cycling times.[26] In the more common flow-between CDI (fbCDI) architecture, the primary flow is through a gap (or porous spacer composed of a porous dielectric bulk material with pores filled with the aqueous electrolyte) between electrode pairs. Hence, in fbCDI cells, the primary directions of ion electromigration and diffusion are commonly orthogonal to ion advection (transport of ions due to bulk flow motion). One-dimensional (1D) solutions of such systems are convenient numerically but woefully incomplete in capturing the coupling of such multidimensional effects.

There have been several recent studies using CDI with various levels of complexity. Biesheuvel et al.[31] developed an adsorption/desorption model tailored for CDI and based on the seminal work of Newman and co-workers on porous electrodes[5−7] and using a classic Gouy−Chapman−Stern (GCS) EDL model. This formulation neglected diffusive transport (assuming well-stirred solution in the gap) and developed a transport model analogous to Ohm's law, where the electric field is the sole driving force. The model resulted in an ordinary differential equation in time and provided no spatial information (spatially zero dimensional or 0D).

In subsequent work, Biesheuvel and Bazant[8] developed a volume-averaged model and explored capacitive charging in porous electrodes. They employed a GCS treatment of EDLs in the absence of Faradaic reaction and without nonelectrostatic ion adsorption. The latter porous electrode model was

Received: June 18, 2015
Revised: August 19, 2015

DOI: 10.1021/acs.jpcc.5b05847
J. Phys. Chem. C XXXX, XXX, XXX−XXX

subsequently extended to include nonelectrostatic ion adsorption and a modified Donnan (mD) treatment of charge layers (e.g., suitable for bimodal porous structures and highly overlapped double layers).[32] In both of the latter studies the models were one dimensional, assuming a quiescent solution between the electrodes and a fixed salt concentration far from the electrodes (e.g., modeling either a separated membrane compartment or a stagnant diffusion layer). Elsewhere, Biesheuvel et al.[33] pointed out that the mD approach remains valid and numerically stable in the limit of very low local salt concentrations. Suss et al.[26] used a 1D porous electrode model with a simple Helmholtz treatment of EDLs and predicted and measured the time evolution of concentration and potential across the gap and electrodes under constant external voltage (i.e., the electric potential applied to the system by an external source) and no-flow conditions. Subsequently, Suss et al.[29] demonstrated in situ spatiotemporal measurements of salt concentration between porous carbon CDI electrodes using an electrically neutral fluorescent probe species and under no-flow (stagnant) conditions. They modeled their CDI cell using a 1D model based on porous electrode theory and an mD treatment of charge capacitance. Rios Perez et al.[12] developed and solved a 1D mass transport model which considered variations along the flow of fbCDI cell. They modeled the transverse flux and subsequent ion adsorption from bulk flow into the electrodes as a local sink term. Their model well predicts the outflow concentration for both low and high flow rates but provides no spatial information throughout the electrodes.

One-dimensional models and models using fixed concentration values at some boundary separated by a stagnant layer are overly simple for CDI cells operated at flowing conditions. To date, we know of no fully two-dimensional (2D) models of CDI cells. The closest approximation of multidimensional effects is perhaps the recent work of Porada et al.[34] The latter group approximated the fbCDI cell under flowing conditions using six 1D electrodes coupled to individual subcells arranged in series along the flow direction. Such treatment is a step toward the capture of the spatial distribution of charge states, but each subcell was assumed to be perfectly stirred—therefore neglecting the coupling of advection and orthogonal diffusive transport.

To the best of our knowledge, there are no theoretical studies which solve *coupled* axial and transverse transports in CDI. There are no 2D ion and transport models in CDI. The spatiotemporal dynamics of such systems are critical to the design and optimized operation of both fbCDI and ftCDI systems. In this paper, we solve, for the first time, a full 2D transport model in an fbCDI cell. We first focus on the formulation of the model, its numerical solution, and experiments associated with model calibration and validation. Our model considers coupled mass transport and ionic and electronic charge transport, including an external, purely resistive parasitic resistance. We strive to simplify the model as much as possible, and our model includes three free parameters. The first is a nonelectrostatic adsorption parameter which captures experimentally observed[9,32] adsorption of salt in the absence of external voltage. The second is a lumped parameter which captures volumetric ionic charge capacitance of the electrodes. The third is the micropore porosity (i.e., the volume fraction of the pores contributing to ion adsorption). To calibrate the model and validate predicted temporal trends, we fabricated a laboratory-scale fbCDI cell with one pair of activated carbon electrodes. Calibration experiments consisted of charging and discharging steps as a function of external voltage under constant flow rate and an open flow loop configuration. We obtained measurements of cumulative adsorbed salt and total electric charge and used these integral measures to fit the associated model predictions using our free parameters. We then fixed these parameters and used the model to predict temporal dynamics of effluent charge concentrations and electric charging current and compared these to temporal measurements. We then present model predictions of unsteady 2D ion concentrations and electric potential within the pressure-driven flow in the gap and within electrodes. Our simulations include both low (20 mM) and relatively high (200 mM) salt concentrations. We investigate the effect of advection, diffusion, and adsorption on the desalination process and identify performance limitations of fbCDI cells including ion starvation and diffusion-limited uptake of salt.

2. THEORY

In this section, we first introduce a double-layer submodel designed for desalination applications and then integrate it into a 2D model based on macroscopic porous electrode (MPE) theory.[5−7] We use this model to capture adsorption and desorption dynamics of charged species in multiscale porous structures.

2.1. Double-Layer Model. We here take the approach of the mD model[9,13,35] to simulate the EDL structure and charge accumulation at the surface of the porous electrode. The mD model approach is more comprehensive than the straightforward EDL model such as Gouy−Chapman−Stern (GCS).[36,37] The GCS model describes the EDL as a combination of an inner, immobile, compact layer (also known as the Stern layer) with constant area-specific capacitance and an outer diffuse layer in which ion distribution is governed by the Gouy−Chapman model. The classic GCS is applicable in the case of nonoverlapping EDLs, wherein the Debye length is small compared to individual pores of the electrode.

We implement a form of the mD model (which describes the electrode double-layer formation) in a formulation applicable to bimodal pore structure electrodes.[29] The model allows for a numerically robust treatment[33] of porous electrodes systems which include a significant volume wherein the characteristic pore diameter is on the order of or smaller than the Debye length and hence overlapped EDLs. Using the typical terminology in CDI, the bimodal pore structure model distinguishes between so-called macropores (pore channels with order 50 nm diameter or larger) and micropores (pore channels with order < 2 nm diameter). The volume occupied by the interconnected macropores is assumed to dominate ion transport throughout the porous electrode, while the micropore volume dominates the regions occupied by EDLs and therefore the capacity for charge accumulation.[29,32,35] The model assumes a quasi-neutral condition (electroneutrality) for ionic concentration in the macropores (i.e., EDLs are negligible in macropore pathways). Further, micropore EDLs include a compact Stern layer immediately adjacent to electrode surfaces. Outside of the Stern layer, the micropore volume is treated as strongly overlapped EDLs (note the Debye length is typically 1−10 nm in CDI systems). As a result, this mD model assumes uniform ion concentration within micropores.

This mD model includes two important deviations from the classical Donnan model: the aforementioned Stern layer and introduction of a treatment for nonelectrostatic adsorption of

DOI: 10.1021/acs.jpcc.5b05847
J. Phys. Chem. C XXXX, XXX, XXX−XXX

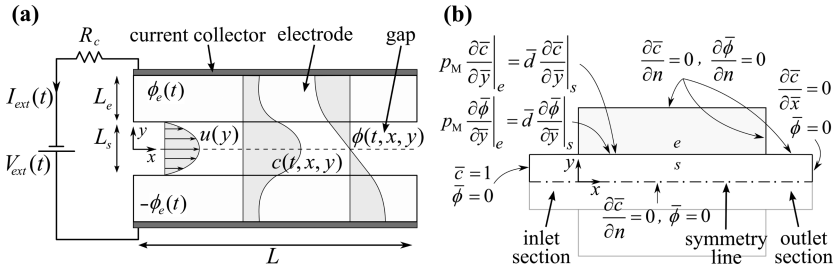

Figure 1. (a) Schematic of elements of our two-dimensional adsorption−desorption and flow model for an fbCDI cell. Two porous carbon electrodes of thickness L_e are sandwiched between two current collectors. Electrodes are separated by a distance L_s to provide space for flow of water (left to right). We lump all contact resistances, e.g., wire to current collector and current collector to electrode connections, into a purely resistive element R_c. (b) Not to scale schematic of computational domain and boundary and interface conditions in nondimensional form. The dash−dot−dash line denotes the geometric symmetry line. The computation domain includes inlet and outlet regions for the flow of length $L/8$.

ions into micropores. The latter assumption has been used in CDI electrode systems which use activated carbon.[32,35] The motivation for this nonelectrostatic treatment is that experimental observations confirm that these materials are known to be significant absorbents of ions even in the absence of external voltage.[38−40] The physics of nonelectrostatic adsorption are not well understood and not well characterized, and the current and previous formulations can be considered empirical corrections of models to account for this effect.

The mD model can be formulated as follows. At chemical equilibrium, there is no electrochemical potential gradient between micro- and macropores. Hence, an extended Boltzmann distribution[41] can be used to relate the micro- and macropore concentration of each species i as

$$c_{m,i} = c_{M,i} \exp\left(-z_i \frac{\Delta\phi_D}{V_T} + \bar{\mu}_{att,i}\right) \tag{1}$$

where $c_{m,i}$ and $c_{M,i}$ are concentration of species i (subscripts m and M denote respectively micro- and macropores parameters), z_i is species valence, $V_T = kT/e$ is thermal voltage (k and T being Boltzmann constant and temperature), $\Delta\phi_D$ is the Donnan potential, and parameter $\bar{\mu}_{att,i} = (\mu_{M,att,i} - \mu_{m,att,i})/kT$ accounts for a nonelectrostatic adsorption potential of ions into micropores. Positive $\bar{\mu}_{att,i}$ may be described as a macro- to microchemical (attraction) potential difference normalized by kT energy. $\bar{\mu}_{att,i}$ may vary for different ions[33,42] or may be a function of the charging state of the system.[43] For simplicity (and to avoid increasing the number of free parameters of our model), we use the same value for all species, i.e., $\bar{\mu}_{att} = \bar{\mu}_{att,i}$, and will use it as one of three free parameters in quantitative comparison to data.

Next, volumetric (net) charge density stored in the micropores $2q_m$ (in units of moles per electrode volume) and micropore potential drop $\Delta\phi_m$ (potential difference between electrode surface and center of the micropore) can be related to micropore capacitance as

$$2q_m F = -C_m \Delta\phi_m \tag{2}$$

where F is the Faraday constant. We here define C_m as the effective volume-specific capacitance of micropores. C_m can be interpreted as the total charge capacitance per unit volume of micropores and includes all EDL structures including Stern layers and/or overlapped diffuse charge layers. This is our second free parameter. Equation 2 shows that the micropore-specific surface area (i.e., total surface area per electrode volume or mass) does not directly appear in the mD model formulation. Instead, we quantify accumulated charge via a volumetric micropore capacitance which characterizes the ion adsorption capacity.[32] There have been several studies presenting models for the accumulated charge in the porous electrodes of CDI cells.[9,29,31] Inspired by empirical observations,[44,45] several recent studies and models have suggested that the effective micropore capacitance in CDI cell electrodes may be a function of micropore charge density and/or micropore potential drop. For example, this dependence has been empirically modeled as[35,46] $C_m = C_S^0 + \kappa_1 q_m^2$ or $C_m = C_S^0 + \kappa_2 \Delta\phi_m^2$, where the first term in each relation was a constant base-value Stern capacitance (at zero net charge) and the second term was an attempt to capture effects of increasing Stern capacitance at higher charge density and/or higher voltages (κ_1 and κ_2 have been assumed constant and positive for the individual cell).

In the current work, we chose to not adopt the latter variable capacitance relations for two reasons. First, we know of no explicit and closed-form relation between micropore capacitance and micropore charge state in this model. Second, removing this treatment results in three (instead of four) fitting parameters for our model. As part of future work, we hope to develop a more self-consistent treatment for micropore capacitance rather than expressing it as an empirical parameter. For example, we hypothesize that other effects such as finite ion size may just as plausibly affect the total micropore capacitance and should be included in capacitance models. For completeness, we note that Biesheuvel et al.[43] studied the ion size effect in the mD model but in the context of relating nonspecific attraction energy to interaction between individual ions and pore surfaces. Lastly, we note our model neglects the effect of surface conduction in all pores and Faradaic reactions within the porous structure.

The third free parameter is macropore porosity p_m, or volume fraction of pores contributing to ion adsorption. We refer the reader to section 2.2 for more discussion. We stress that the aforementioned, three-parameter mD model is just one of several EDL-type charge capacity models which can be applied to CDI systems. Our formulation (see section 2.2) is sufficiently modular, so that the current transport model can be readily modified using a modified and/or improved EDL model (e.g., using additional parameters). Overall, the formulation for the specific charge capacitance of the CDI system as formulated here has three free parameters, $\bar{\mu}_{att}$, C_m, and p_m. We extract these parameters by performing a series of experiments on a flow-between CDI cell under constant voltage conditions (see Experimental Setup and Methods and Experimental Results below).

DOI: 10.1021/acs.jpcc.5b05847
J. Phys. Chem. C XXXX, XXX, XXX−XXX

2.2. Transport Equations in Flow-Between CDI Cell. Our main focus here is investigation of the ion and bulk flow transport dynamics in fbCDI cells. A not to scale schematic of our two-dimensional fbCDI cell is shown in Figure 1a. The cell consists of two porous carbon electrodes sandwiched between two highly conductive current collector plates (on top and bottom), and feedwater flows in the space between the electrodes from left to the right. We assume the space (or gap) region between electrodes is completely filled with feedwater, although we note it is simple to extend our model to include simple Darcy flow through a porous spacer region. As in a typical fbCDI cell, we assume the gap thickness, L_s, is much smaller than the electrode spanwise (into the page) width W. This allows us to avoid the complexity of three-dimensional velocity field and, hence, to use a fully developed parabolic velocity profile (Poiseuille flow) in the space region.

The contact resistance associated with the interface between the current collectors and the electrodes can be a dominant portion of total resistance of a typical CDI cell.[47] Thus, we here include a purely resistive element, R_c, to model this effect (the capacitance of the contact is negligible compared to that of the electrode). We further neglect the resistance of the solid portions of the electrode matrix, as we estimate this is much smaller than typical electrolyte resistances. We lump any other external resistances (e.g., connecting wires) as in series with the contact resistance and thus part of the parameter R_c. To the best of our knowledge, this is the first solution of a full two-dimensional model for an fbCDI system.

In a manner similar to classical MPE theory, we formulate transport equations on a volume average basis.[5−7] Volume averaging is performed over a length scale considerably larger than macropore features but small enough to capture the spatiotemporal variation of electric potential and species concentrations.[5,7,8] This avoids detailed treatment of the complex morphology of porous structures and models the ionic adsorption/desorption effects into sink/source terms within the governing equations. We start with the general form of the mass transport equation without reaction for species i as

$$\frac{\partial c_i}{\partial t} + \nabla\cdot\boldsymbol{j}_i = 0 \tag{3}$$

where c_i is the concentration of species i and $\boldsymbol{j}_i$ is its associated molar flux vector with electromigration, diffusion, and advection contributions as

$$\boldsymbol{j}_i = c_i\boldsymbol{u} - \frac{z_i D_i}{V_T} c_i \nabla\phi - D_i \nabla c_i \tag{4}$$

where $\boldsymbol{u}$ is the bulk velocity vector, D_i is the diffusion coefficient of species i, and ϕ is the local electric potential. We assume a dilute, binary, symmetric, and univalent electrolyte ($z_i = \pm 1$) with equal anion and cation mobilities and thus equal diffusion coefficients. We also assume fully developed parabolic velocity profile $\boldsymbol{u} = u(y)\hat{\mathbf{x}}$ within the gap region. By adding and subtracting eq 3 for $i = \pm 1$ and using electroneutrality approximation in the gap, the conservation of salt and charge in this region is simply governed by the advection−diffusion equation $\partial c/\partial t + u(y)\partial c/\partial x = D\nabla^2 c$ and Ohm's law $\nabla\cdot(c\nabla\phi) = 0$, where c is the concentration of co- and counterions in bulk solution and in macropores (i.e., $c = c_i$). We assume symmetric electrolyte, so $D = D_i$ for $i = \pm 1$. In our bimodal pore structure electrode, ion transport in macropores can be described as[35]

$$\frac{\partial}{\partial t}(p_M c_{M,i} + p_m c_{m,i}) + \nabla\cdot\left[c_{M,i}\boldsymbol{u}_{sup} - p_M D_{e,i}\left(\nabla c_{M,i} + \frac{z_i}{V_T} c_{M,i}\nabla\phi\right)\right] = 0 \tag{5}$$

where p_m and p_M are, respectively, the porosity of micro- and macropores and are related to total electrode porosity p as $p_M + p_m = p$. We measured the total porosity of our electrode as approximately 0.7 using dry/wet-saturated mass measurement. Equation 5 is consistent with porosities that are defined as pore volume per the total macroscopic volume of electrode and not per volume of electrode solid (carbon). In the macropores, electroneutrality holds, and thus, $c = c_{M,i}$ for $i = \pm 1$. In micropores, however, the difference between co- and counter-ion concentrations balances the wall surface charge density. $\boldsymbol{u}_{sup}$ is a superficial flow velocity throughout the pores, defined as the flow rate per total cross-section area. $D_{e,i}$ is the effective diffusion coefficient of species in macropores and in general differs from that of the free solution due the effect of porosity and tortuosity.[48−51] For simplicity, we here assume a value of $D_{e,i}/D_i = 0.5$ for both species. This is an approximate but reasonable estimate according to the reported empirical correlations for porous materials, including porous electrodes, with porosities in the range of 0.6−0.8.[48,52]

In the macropores, we set $\boldsymbol{u}_{sup} = 0$. This means we neglect all bulk flow (e.g., pressure-driven Darcy-type flow or any electrohydrodynamic flow) within the electrode. The latter assumption is equivalent to assuming the permeability of the electrodes is negligible compared to the effective (open channel) permeability of the gap region. For simplicity, we further neglect electroosmotic flow (and any pressure-driven flow associated with nonuniform electroosmotic flow) within the porous electrodes. We hypothesize that the latter may be important in some systems and suggest it as a topic for future work. With these assumptions, the governing equations for salt and charge balance (derived from eq 5 by adding and subtracting equations for $i = \pm 1$) can be expressed as

$$\frac{\partial c}{\partial t} = D_e\nabla^2 c - \frac{p_m}{p - p_m}\frac{\partial w_m}{\partial t} \tag{6}$$

$$\nabla\cdot(c\nabla\phi) = \frac{p_m}{p - p_m}\frac{V_T}{D_e}\frac{\partial q_m}{\partial t} \tag{7}$$

where $2w_m = c_m^+ + c_m^-$ is the volumetric ions concentration and $2q_m = c_m^+ - c_m^-$ is the (net) charge density in micropores (each with units of moles per electrode volume). Assuming electrochemical equilibrium for micropore double layers throughout the electrode, anion (cation) expulsion in the micropores of negative (positive) electrode leads to an electric potential mismatch between macro- and micropores. This potential difference is the well-known Donnan potential $\Delta\phi_D$. The potential difference between electrode matrix and pore solution is related to micropore potential drop $\Delta\phi_m$ and Donnan potential as

$$\phi_e - \phi = \Delta\phi_m + \Delta\phi_D \tag{8}$$

where ϕ_e is the time varying but spatially uniform potential of the upper electrode. Due to symmetry, the other electrode has potential $-\phi_e$. Thus, the cell voltage (voltage difference between the upper and lower electrode) can be written as $V_{cell} = 2\phi_e$.

DOI: 10.1021/acs.jpcc.5b05847
J. Phys. Chem. C XXXX, XXX, XXX−XXX

Next, we nondimensionalize the governing equations as $x = L\bar{x}$, $y = L_e\bar{y}$, $t = \bar{t}L_e^2/D_e$, $\phi = V_T\bar{\phi}$, $c = c_0\bar{c}$, $q_m = c_0\bar{q}_m$, and $w_m = c_0\bar{w}_m$, where L, L_e, and c_0 are the length and thickness of electrodes and the inlet and initial concentration of solution, respectively. The final set of equations describing the adsorption/desorption process inside the electrodes is

$$\frac{\partial \bar{c}}{\partial \bar{t}} = \bar{\nabla}^2\bar{c} - \frac{p_m}{p - p_m}\frac{\partial \bar{w}_m}{\partial \bar{t}} \tag{9}$$

$$\bar{\nabla}\cdot(\bar{c}\bar{\nabla}\bar{\phi}) = \frac{p_m}{p - p_m}\frac{\partial \bar{q}_m}{\partial \bar{t}} \tag{10}$$

$$\bar{q}_m = -\bar{c}\,\exp(\bar{\mu}_{att})\sinh(\Delta\bar{\phi}_D) \tag{11}$$

$$\bar{w}_m = \bar{c}\,\exp(\bar{\mu}_{att})\cosh(\Delta\bar{\phi}_D) \tag{12}$$

$$\bar{\phi}_e - \bar{\phi} = -2F\bar{q}_m/\bar{C}_m + \Delta\bar{\phi}_D \tag{13}$$

and the following apply to the gap region

$$\frac{\partial \bar{c}}{\partial \bar{t}} + \alpha_e Pe_e \bar{u}\frac{\partial \bar{c}}{\partial \bar{x}} = \bar{d}\bar{\nabla}^2\bar{c} \tag{14}$$

$$\bar{\nabla}\cdot(\bar{c}\bar{\nabla}\bar{\phi}) = 0. \tag{15}$$

Nondimensional effective micropore capacitance, $\bar{C}_m$, is defined as $\bar{C}_m = C_m V_T/2Fc_0$, $\bar{u} = u/U$ is bulk flow velocity normalized by the mean flow velocity, $\alpha_e = L_e/L$ is the geometric aspect ratio of the electrode to flow region length, $Pe_e = UL_e/D_e$ is the Peclet number based on the electrode thickness, and $\bar{d} = D/D_e$ is the ratio of diffusion coefficients in the gap to the pore region.

On the basis of eqs 9, 10, and 14, there are three fundamental time scales associated with the fbCDI system. First is the diffusion time of ions across the electrode, L_e^2/D_e. The second is a resistive-capacitive (RC) time scale associated with micropore charging. The latter can be written as p_m/p_M and normalized by the diffusion time across the electrode thickness. This RC time scale characterizes the time evolution of charge and salt adsorption within the electrode (see eqs 9 and 10). Third is an advective time scale associated with the feedwater flow (and ion advection) within the gap. The parameter $\alpha_e Pe_e$ in eq 14 is simply the ratio of (transverse) diffusion time across the electrode thickness to the advection time of the stream. This compares the rates of axial advection and transverse diffusion.

A schematic of the computational domain is shown in Figure 1b. Our model includes inlet and outlet sections of lengths $L/8$ in the computational domain. These enable us to impose inlet and outlet boundary conditions sufficiently far from electrode edges. We set concentration as uniform at the inlet and assume zero concentration gradient at the outlet. The inlet and outlet boundaries assume zero electric potential. We performed a limited number of numerical experiments using inlet and outlet regions of longer length to confirm that the $L/8$ additions to the computational domain were sufficient to avoid end effects.

Boundary and interface conditions (also shown in Figure 1b) are as follows: (1) Zero mass and current flux across side walls of the inlet and outlet sections and across the outer boundaries of the electrodes (left, right, and top sides of the electrode in Figure 1b), (2) uniform concentration at the inlet, (3) advective boundary condition for concentration at the outlet, (4) zero electric potential at the inlet and outlet (refer to section S6 of the Supporting Information for further discussion of these boundary conditions), and (5) continuity of concentration and potential as well as (6) salt flux (i.e., $p_M\,(\partial\bar{c}/\partial\bar{y})_e = \bar{d}(\partial\bar{c}/\partial\bar{y})_s$) and electric current (i.e., $p_M\,(\partial\bar{\phi}/\partial\bar{y})_e = \bar{d}(\partial\bar{\phi}/\partial\bar{y})_s$) at the electrode−solution interface. The interface conditions for salt flux and electric current at the solution side are multiplied by p_M in order to correct for the effect of macropore porosity. Our assumption of a binary, symmetric electrolyte results in a geometric symmetry about the midplane of the gap region. This and the boundary conditions result in symmetry of the spatiotemporal concentration fields and an antisymmetry of potential. We take advantage of this to only model the geometrically symmetric (top) half of the CDI cell.

We couple the desalination system to an external circuit by incorporating a contact resistance. Kirchhoff's law relates the external voltage and current as

$$\bar{V}_{cell} = \bar{V}_{ext} - \bar{r}_c\bar{i}_{ext} \tag{16}$$

where $\bar{V}_{cell} = V_{cell}/V_T$, $\bar{V}_{ext} = V_{ext}/V_T$, $\bar{i}_{ext} = I_{ext}/I_0$, and $\bar{r}_c = R_c/R_0$ are nondimensional cell voltage, external voltage, external current, and contact (and other external series) resistance, respectively, and $R_0 = V_T/I_0 = V_T L_s/2Fc_0DLW$. To close the system of equations, we seek a relation between external current $\bar{i}_{ext}$ as a cumulative quantity to other parameters of the model. We note that macropore ionic current is not divergence free throughout the electrode, as there is a net charge transfer to and from the micropores. Macropore ionic current $\boldsymbol{i} = Fz(\boldsymbol{j}_+ - \boldsymbol{j}_-)$, after correcting for porosities, can be related to micropore charge flux as $p_M\,\nabla\cdot\boldsymbol{i} = -2p_mF(\partial q_m/\partial t)$. External current I_{ext} can thus be found, equivalently, by integrating micropore charge flux over the entire electrode volume as $\int\int 2p_mF(\partial q_m/\partial t)W\,dx\,dy$ or ionic current passing through the electrode−solution interface as $\int(2p_MFD_e/V_T)(c\,\partial\phi/\partial y)W\,dx$. For the latter, we simply used the divergence theorem to recast the surface integral to a line integral along the interface. Thus, the nondimensional form of external current can be written as

$$\bar{i}_{ext} = \frac{p_m}{\bar{d}}\iint\frac{\partial \bar{q}_m}{\partial \bar{t}}\,d\bar{x}\,d\bar{y} = -\frac{p_M}{\bar{d}}\int_0^1 \bar{c}\frac{\partial\bar{\phi}}{\partial\bar{y}}\,d\bar{x} \tag{17}$$

The surface integral above simply states that total electron current to the system is equal to the volume integral of time derivative of spatiotemporal adsorbed charge within the micropores. Equations 16 and 17 couple the external circuit to the desalination system and along with eqs 9−15 fully describe adsorption/desorption dynamics. The governing equations in this section are also applicable to alternate treatments of the EDL and/or micropore charge relations by replacing eqs 11−13 with a set of equations describing the alternate model. Further, eqs 16 and 17 should also allow for modeling adsorption/desorption dynamics under any constant or time-dependent voltage- and current-controlled operation.

2.3. Equilibrium Solution. In this section, we focus on a solution of the model discussed above at equilibrium (i.e., at infinitely long time). The equilibrium solution is governed solely by the EDL submodel, external voltage, and inlet concentration. Other parameters such as the system geometry, flow rate, or shape of the velocity profile do not affect the equilibrium behavior of the system. At a time much longer than the largest time scale of the system, salt concentration becomes uniform throughout the gap and macropores. Moreover, the electric potential of the solution and total electric current both approach zero. By combining eqs 2, 11, 13, and 16 and using

DOI: 10.1021/acs.jpcc.5b05847
J. Phys. Chem. C XXXX, XXX, XXX−XXX

the symmetry assumption, we arrive at the following transcendental equation for the equilibrium Donnan potential

$$\frac{V_{ext}}{2V_T} = \Delta\bar{\phi}_D + \frac{2Fc_0}{C_m V_T}\exp(\bar{\mu}_{att})\sinh(\Delta\bar{\phi}_D) \quad (18)$$

where c_0 is the inlet salt concentration. Equation 18 has a guaranteed unique solution (for which we define as $\Delta\bar{\phi}_D^{\infty}$) as the right-hand side is strictly monotonic with respect to the Donnan potential. We term the resulting (characteristic) micropore salt and charge w_m^{∞} and q_m^{∞}, respectively. The near-equilibrium total adsorbed salt and transferred electronic charge (in units of moles and Coulombs, respectively) can then be written as

$$2p_m(w_m^{\infty} - w_m^0)V_e = 2c_0 p_m \exp(\bar{\mu}_{att})(\cosh(\Delta\bar{\phi}_D^{\infty}) - 1)V_e \quad (19)$$

$$2Fp_m q_m^{\infty} V_e = -2Fc_0 p_m \exp(\bar{\mu}_{att})\sinh(\Delta\bar{\phi}_D^{\infty})V_e \quad (20)$$

Here, V_e is the electrode volume and $w_m^0 = c_0 \exp(\bar{\mu}_{att})$ is the initial adsorbed charge at zero external voltage due to nonelectrostatic adsorption of ions. Close inspection reveals that, for the equilibrium solution, our three fitting parameters ($\bar{\mu}_{att}$, C_m, and p_m) reduce to just two independent groups: $p_m C_m = C_m^*$ and $p_m \exp(\bar{\mu}_{att}) = \exp(\bar{\mu}_{att}^*)$. As will be described in section 4.1, we use experimental equilibrium conditions to extract these two groups from our measurements. As described in section 4.1, we subsequently use dynamic measurements (including the temporal profile of effluent salt concentration) to fix the third independent parameter p_m.

3. EXPERIMENTAL SETUP AND METHODS

We designed and fabricated a custom-built, mesoscale fbCDI cell using a pair of activated carbon electrodes and performed a series of constant voltage, continuous-flow experiments. We used these experiments to validate selected trends predicted by our two-dimensional model and to extract free parameters $\bar{\mu}_{att}$, C_m, and p_m.

3.1. CDI Cell Design. We fabricated an fbCDI cell using a pair of activated carbon electrodes (Material Methods, PACMM, Irvine, CA) with dimensions of 100 × 20 × 0.68 mm and total dry mass of 1.42 g. We stacked the electrodes between two 100 × 20 × 0.2 mm stainless steel plates, which acted as current collectors (see Figure 2). To improve electric contact between the porous electrodes and the current collectors,[47] we adhered the electrodes to these plates using silver conductive epoxy (MG Chemicals, cat No. 8331-14G, Surrey, BC, Canada). In addition to silver epoxy, we observed that electrode compression significantly reduces the electrode-current collector resistance. Our design had four compression slot features (see Figure S1 of the Supporting Information) to compress the peripheral regions of electrode. We used plastic shim features (not shown in Figure 2) between the compressed parts of electrodes to avoid electrical shorting. We refer reader to the Supporting Information (Figure S1) for more details. We also adhered the connecting wires to the current collectors with silver epoxy. This assembly was then housed inside a 3D-printed (ProJet HD 3000 Plus, 3D Systems, Rock Hill, SC) clamshell structure and sealed with gaskets and fasteners. The housing and seals held the electrodes a distance of 0.8 mm apart in the absence of any porous spacer. The upper clamshell was connected to two 1/8 in. outer diameter stainless steel tubes (Scanivalve, Liberty Lake, WA) which served as water inlet and outlet.

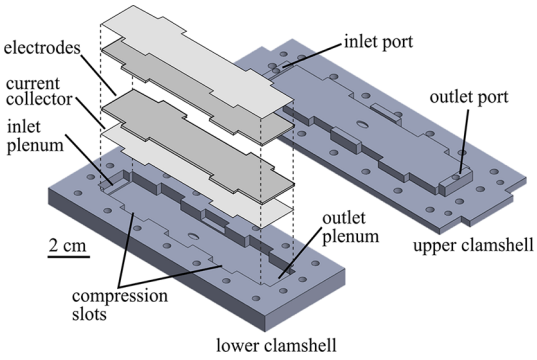

Figure 2. Three-dimensional drawing of our CDI cell clamshell structure. We sandwiched a pair of activated carbon electrodes inside the upper and lower clamshells and sealed the desalination cell using a gasket and fasteners (not shown). Electrodes have dimensions of 100 × 20 mm with 0.68 mm thickness. Our design had inlet and outlet plenum chambers in order to uniformly introduce salt solution to and collect desalted water from the CDI cell. See Figure S1 of the Supporting Information for more details.

Our cell had inlet and outlet plenum chambers which were used, respectively, to distribute salt solution from inlet port to electrode gap and to guide desalted water from the gap toward the outlet port (see Figure 2). Minimizing the volume of the chambers is essential in any CDI cell design, as this reduces the dispersion effect (a phenomenon in which salt and fresh water solution actively mix to each other and produce a solution with intermediate salt concentration). We estimated the dead volume of our cell (volume of inlet and outlet plenum chambers) to be <0.1 mL, while total gap volume was 1.6 mL. This suggests that the effects of dispersion within the inlet and outlet chambers was negligible.

3.2. Experimental Procedure. We used potassium chloride (KCl) to approximate a binary, symmetric, and univalent solution. Potassium and chloride ions have roughly equal electrophoretic mobility (76.2×10^{-9} and 67×10^{-9} m^2 V^{-1} s^{-1} in free solution and room temperature[53,54]). KCl has been used in other work for CDI experiments for this reason.[29] We used 20 mM influent salt concentration for two reasons. First, this low concentration enabled investigation of regimes associated with very significant ion depletion and hence strong, easily measurable removal of ions. It also enables more detailed study of diffusion-limited desalination regimes (typical of fbCDI). Second, desalination of moderate salt concentrations (10−100 mM) is common in experimental CDI studies,[10,31,33,55−62] and these serve as comparison cases. In section 5.2, we present simulations in higher concentrations (200 mM) and compare the results to the low-concentration case.

We performed a series of preliminary wash and charge/discharge cycles prior to the experiments. The washing procedure was as follows. We filled the cell with 20 mM KCl and let it stand for 24 h prior to starting experiments. To reduce the effect of nonspecific interaction of ions with pristine electrodes, we performed 18 consecutive charge−discharge cycles by applying 1.2 V (for 30 min) for charging and 0 V (for 1 h) for discharging (Keithley 2440 sourcemeter, Cleveland, OH) at 0.42 mL min^{-1} flow rate (Watson Marlow peristaltic pump, Wilmington, MA). After this aging process, we pumped 20 mM KCl solution again for 6 h with no external potential in

DOI: 10.1021/acs.jpcc.5b05847
J. Phys. Chem. C XXXX, XXX, XXX−XXX

an effort to flush out loosely adsorbed ions. The feedwater used was not purged with nitrogen gas.

At this point, we started desalination experiments. We used 0.42 mL min^{-1} constant flow, and we applied an external voltage of 0.4, 0.6, 0.8, and 1 V (in ascending order) across the cell. For each voltage, we charged the cell for 2 h and discharged the cell at 0 V for 3 h. The charging and discharging times were chosen such that the effluent concentration asymptotes to around 90% of the inlet value. We performed two successive charge/discharge cycles for each external voltage.

For each experiment, we recorded a time series of electric current and effluent conductivity using, respectively, the Keithley sourcemeter and a calibrated flow-through conductivity sensor (eDAQ, Denistone East, Australia). The conductivity sensor had ~93 μL internal channel volume. Conductivity was converted to salt concentration using a calibration curve for KCl. As described below, we used these current and concentration measurements to evaluate the free parameters of our fbCDI cell (cf. section 4.1 for more information).

4. EXPERIMENTAL RESULTS

Here, we first define two desalination metrics and show their experimental values. We compare these measured quantities to model predictions. We then find the values of free parameters by minimizing the error between experiments and model results. We performed all numerical simulations with COMSOL Multiphysics (version 4.5, COMSOL Inc., Burlington, MA) using transport of diluted species and equation-based modeling interfaces.

4.1. Parameter Extraction. We used electric current and effluent concentration measurements to estimate near-equilibrium adsorbed salt and transferred electric charge during CDI charging (i.e., total electronic charge supplied from the external power source). To this end, we performed the aforementioned set of experiments to quantify these as a function of external voltage. We then compared these measured quantities to corresponding values predicted using our model.

We first describe our estimate of cumulative salt adsorbed during charging. For a finite charging time t, salt absorbed can be expressed as follows

$$\Gamma(t) = \frac{1}{m_{tot}} \int_0^t Q(c_0 - \langle c_{out}(\tau)\rangle)\mathrm{d}\tau \tag{21}$$

where Q is the water flow rate, $\langle c_{out}\rangle$ is the outlet-area-averaged effluent concentration (defined as $\int u c_{out}\,\mathrm{d}y / \int u\,\mathrm{d}y$), and m_{tot} is total dry mass of the electrodes. For our predictions, we integrate the outlet concentration for each simulated time to calculate $\langle c_{out}\rangle$ under constant flow rate conditions. In the experiments, our downstream conductivity sensor directly quantifies $\langle c_{out}\rangle$, also under constant flow rate conditions. The adsorbed salt (per electrodes mass) can also be expressed in volume integral as follows

$$\Gamma(t) = \frac{1}{m_{tot}} \iint 2p_m(w_m(t) - w_m^0)W\,\mathrm{d}x\,\mathrm{d}y \tag{22}$$

These two forms are indeed numerically equivalent (and we confirmed this with our numerical model). At each external voltage, we integrated the measured cumulative salt over time during 2 h charging. We call this near-equilibrium salt Γ_{eq} and show the corresponding measured values in Figure 3a. This figure indicates that salt adsorption capacity increases (almost linearly) with external voltage.

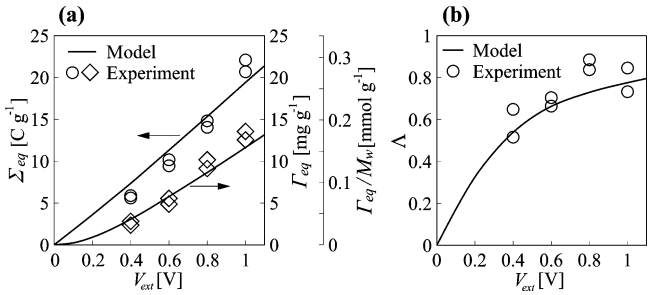

Figure 3. (a) Near-equilibrium adsorbed salt and transferred charge (per mass of electrodes) and (b) charge efficiency, $\Lambda = F\Gamma_{eq}/M_w\Sigma_{eq}$, for 2 h of constant voltage operation in the range from 0 to 1 V and flow rate of 0.42 mL min^{-1}. Feedwater inlet concentration is 20 mM KCl. Open circles and diamonds are measured data, and solid lines are model prediction. Charge efficiency approaches unity as voltage increases, indicating stronger asymmetry in the micropore counterion adsorption and co-ion expulsion.

Next, we define cumulative transferred electronic charge—or equivalently, cumulative adsorbed ionic charge—relative to zero external voltage on a per electrodes mass basis as

$$\Sigma(t) = \frac{1}{m_{tot}} \int_0^t (I_{ext}(\tau) - I_{leak})\mathrm{d}\tau \tag{23}$$

where leakage current, I_{leak}, is a nonzero current measured even long after starting the charging step and likely associated with unwanted Faradaic reactions at the electrode surface.[63] Cumulative charge can also be presented as follows

$$\Sigma(t) = \frac{1}{m_{tot}} \iint 2Fp_m q_m(t)W\,\mathrm{d}x\,\mathrm{d}y \tag{24}$$

We again integrated the measured cumulative charge over 2 h charging time. We call this value near-equilibrium charge (Σ_{eq}) and also show its experimental measurements in Figure 3a. Similar to Γ_{eq}, variation of Σ_{eq} is also almost linear with external voltage. Further, we note that Γ_{eq} and Σ_{eq} are only a function of external voltage and not the operational parameters such as flow rate.

As discussed in section 2.3, the equilibrium results do not provide sufficient information for parameter extraction. As a result, we used effluent salt concentration data as well. We first used measured equilibrium salt and electrical current to evaluate two unknown parameter groups (see section 2.3 for more details). To this end, we varied $p_m C_m$ and $p_m \exp(\bar{\mu}_{att})$ (as two independent groups) and minimized the sum of squares of model prediction and measured equilibrium values of salt and charge. Subsequent to this, we used the dynamic data to obtain p_m. To this end, we varied p_m (while maintaining $p_m C_m$ and $p_m \exp(\bar{\mu}_{att})$ constant) such that the effluent salt concertation from model matched that of the recorded data. Our final estimated parameters are as follows: $\bar{\mu}_{att} = 1.5$, $C_m = 150$ MF m^{-3}, and $p_m = 0.3$. All predictions presented below use the same three values of this parameter. These values are close to those reported for similar activated carbon electrode materials[64] and for hierarchical carbon aerogel monolith (HCAM) electrodes.[29] A complete list of parameter settings used in the model is presented in Table 1. As shown in Figure 3a, there is a reasonable agreement between data and model predictions for

DOI: 10.1021/acs.jpcc.5b05847
J. Phys. Chem. C XXXX, XXX, XXX−XXX

Table 1. Parameter Settings for the Two-Dimensional Model for an fbCDI Cell Incorporating mD EDL Model and Operated in Constant External Voltage and Flow Rate[a]

parameter	description	value	unit
$\bar{\mu}_{att}$	nonelectrostatic adsorption parameter	1.5	
C_m	micropore capacitance	150	MF m^{-3}
p_m	micropore porosity	0.3	
p_M	macropore porosity	0.4	
D	diffusion coefficient in the gap	1.9×10^{-9}	m^2 s^{-1}
D_e	effective diffusion coefficient in macropores	0.95×10^{-9}	m^2 s^{-1}
c_0	influent salt concentration	20	mM
R_c	contact resistance	4.7	Ω
U	mean flow velocity	4.38×10^{-4}	m s^{-1}
L_s	gap thickness	0.8	mm
L	electrode length	100	mm
L_e	electrode thickness	0.68	mm
W	electrode width	20	mm

[a]The cell consists of a pair of activated carbon electrodes stacked between two current collectors and separated by a gap.

these model parameters. We see a deviation between model and experimental data for external voltages higher than about ~1.2 V. We attribute this discrepancy primarily to the effects of Faradaic reactions at these higher potentials (which is not captured by the present model).

4.2. Charge Efficiency. As mentioned above, Figure 3a shows near-equilibrium adsorbed salt Γ_{eq} and transferred charge Σ_{eq} (the associated cumulative quantities evaluated at the end of 2 h charging process) as a function of external voltage for both model and experiments. In Figure 3b we show the ratio of these metrics, $\Lambda = F\Gamma_{eq}/M_w\Sigma_{eq}$, known as charge efficiency (M_w being the salt molecular weight). The electric current applied to the cell results in both accumulation of counterions (within micropores) and repulsion of co-ions. Hence, charge efficiency characterizes the ratio of accumulated charge (as bound ions) to the integral of electric current.[65,66] For small external voltage (e.g., in Debye–Hückel limit), the amount of counterion adsorption into the diffuse double layer is approximately the same as the amount of co-ion expulsion. However, higher potentials break this symmetry and so increase charge efficiency. The latter trend is reflected in the data of Figure 3b.

4.3. Temporal Results. Figure 4 shows evolution of effluent salt concentration (normalized by 20 mM KCl inlet concentration) in charging and discharging processes for experiments and model. We here use the parameter setting identical to those in Table 1 without any additional fitting parameter. Results are shown for charging up to $\bar{t} = 14$ (equivalent to about 2 h) followed by discharging up to $\bar{t} = 28$ and for four external voltages of 0.4, 0.6, 0.8, and 1 V. Time is normalized by the diffusion time scale across the electrode thickness, L_e^2/D_e, which is order 500 s based on Table 1. Figure 4 shows a fairly rapid drop in the outlet concentration at around $\bar{t} = 0.5-1$ followed by a slowly increasing concentration phase. The initial rapid phase of the charging process corresponds to fast (RC time scale) adoption of ions originally inside macropores. The adsorption process is then slowed down by diffusion-limited uptake of new ions from the gap, which, in turn, results in gradual increase of outlet salt concentration. We discuss this adsorption process in more detail in section 5.2. The discharging process shows a similar

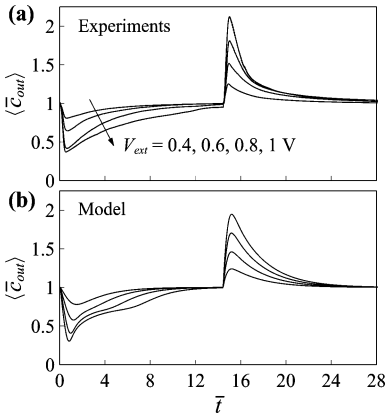

Figure 4. (a) Measured and (b) model predicted normalized effluent salt concentration vs time (normalized by diffusion time L_e^2/D_e) for constant voltage operation at 0.4, 0.6, 0.8, and 1 V and constant flow rate of 0.42 mL min^{-1}. Feedwater concentration is 20 mM KCl, and time is normalized by diffusion time scale across the electrode thickness.

trend: an initial fast desorption followed by a gradual decrease of concentration. This two-phase adsorption/desorption is typical of fbCDI systems and has been observed experimentally and computationally.[26,29] In this figure, the model follows the overall trend of experiments; however, it only approximately matches the measured data. We attribute the discrepancies to two main sources. First is our assumption of constant micropore capacitance is not sufficiently precise. As we mentioned in section 2.1, we hypothesize that the model can be improved by (explicitly) relating the micropore capacitance to the micropore charge state. Second, the method of model calibration using mainly the equilibrium measurements, which is commonly used in CDI,[29,46] neglects the exact dynamic behavior of the system. We hypothesize that additional ex-situ characterization may help better characterize the electrode material. For example, electrochemical impedance spectroscopy[67–69] and cyclic voltammetry[70–72] may be employed to extract a more accurate and voltage-dependent micropore capacitance. Further, in Figure 5 we present the time evolution of cumulative adsorbed salt $\Gamma(t)$ and cumulative transferred electric charge $\Sigma(t)$ during charging for voltages similar to those in Figure 4. We again see that the model follows the observed trends fairly well, but it is not in perfect agreement with the experiments.

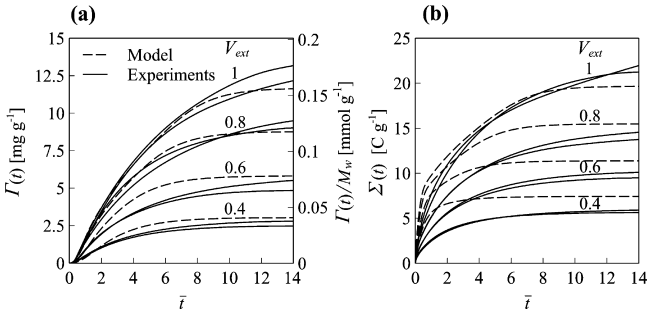

Figure 5. (a) Cumulative stored salt $\Gamma(t)$ (mg g^{-1}) and (b) electric charge $\Sigma(t)$ (C g^{-1}) vs normalized time for ~2 h of charging for constant external voltage operation at 1 V and flow rate of 0.42 mL min^{-1}. Each is reported per electrode dry mass.

DOI: 10.1021/acs.jpcc.5b05847
J. Phys. Chem. C XXXX, XXX, XXX–XXX

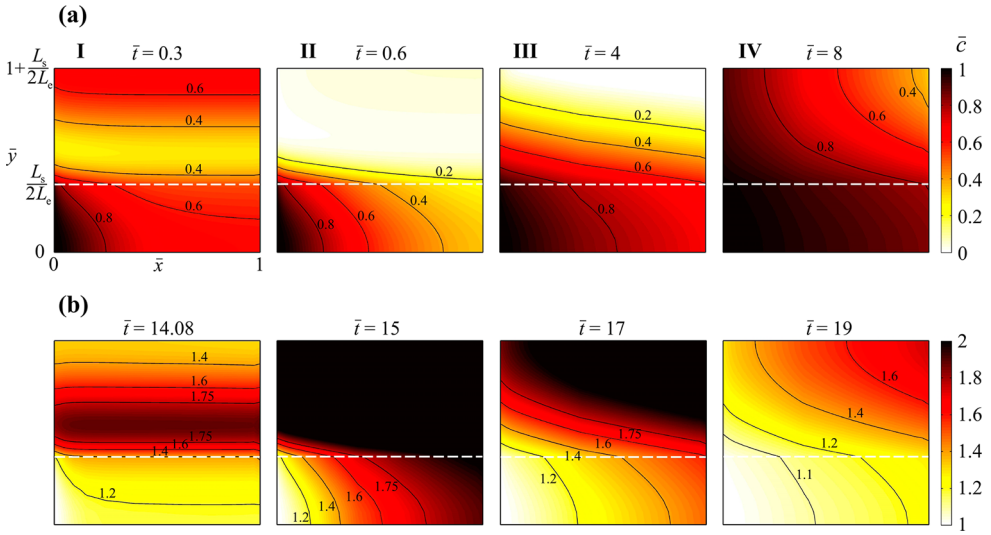

Figure 6. Normalized ion concentration fields in the gap and macropores for the symmetric top half of the cell (not to scale) for constant voltage (a) charging (1 V) and (b) discharging (0 V) (as per Table 1). Dashed lines indicate the electrode−solution interface. Time is normalized by the diffusion time scale associated with the electrode thickness. In charging, a depletion region forms near and propagates upward from the electrode−solution interface. This rapid charging is followed by a slow, diffusion-limited uptake of new ions from the gap. At the beginning of discharge, formerly adsorbed ions (now have same sign of charge as electrode) are quickly electrostatically repelled from micropores in the near-gap region. This forms a near-gap depletion region whose boundary then propagates upward. Discharge then slows down significantly as the cell proceeds into a diffusion-limited transport of ions out of the electrode. A movie animating the spatiotemporal fields of our 2D model is available as the Supporting Information.

5. SPATIOTEMPORAL RESULTS

In section 4, we discussed the process by which we evaluated the free parameters of our unsteady, 2D model. We here focus on this model's predictions of two-dimensional spatiotemporal concentration and electric potentials during charging and discharging.

5.1. Macropore Concentration. Figure 6 shows normalized concentration profiles in the gap ($0 < \bar{y} < L_s/2L_e$) and electrode region ($L_s/2L_e < \bar{y} < 1 + L_s/2L_e$) of the cell (collectively the top symmetric half of the cell) at selected times for 0.42 mL min^{-1} flow rate. In the electrode region, we plot the concentration of ions in the (net neutral) macropores. The figure shows color maps and contours of concentration during charging at V_{ext} = 1 V in the top row and for discharging at V_{ext} = 0 in the bottom row. The dashed line at $\bar{y} = L_s/2L_e$ represents the electrode−solution interface. The less interesting inlet and outlet sections (cf. Figure 1b) are not shown here. Time is normalized by the diffusion time scale across the electrode thickness, L_e^2/D_e, which is on the order of 500 s for the parameters listed in Table 1.

In this section we describe simulation cases for 20 mM KCl inlet concentrations. We summarize a simulation at 200 mM in the next section. The cell is charged to $\bar{t}$ = 14 (equivalent to about 2 h) at 1 V and then discharged at 0 V, all with total plotted run time of $\bar{t}$ = 19. The figure shows concentration fields at charging times $\bar{t}$ = 0.3, 0.6, 4, and 8 and discharge times $\bar{t}$ = 14.08, 15, 17, and 19. We also provide videos of the full spatiotemporal concentration fields as the Supporting Information. Figure 6a-I shows that, shortly after application of external voltage, a near-gap depletion zone forms within the electrode. This low-concentration region grows, and its boundary propagates toward the top of the electrode at $\bar{y} = 1 + L_s/2L_e$. The salt adsorption capacity of our cell at 1 V is approximately 4.5 times greater than the initial salt contained within the total cell volume. Thus, macropore concentration decreases to order $\bar{c} \approx 0.001$ shortly after charging at 1 V (within about $\bar{t}$ = 1, or about 8 min after charging starts). We refer to this phenomenon as electrode starvation, where the simulated local macropore concentration approaches zero. This rapid ion-depletion phase, however, does not lead to fully charged micropores throughout the electrode. For example, at $\bar{t}$ = 1 only 15% of micropores are more than 80% charged, while 50% of them have a charge state less than 30% of their maximum (see Figure S4 for a plot of micropore counterion concentration). We discuss this phenomenon in more detail in section 5.3.

After $\bar{t}$ = 1, the micropores continue to charge and deionization continues. This relatively slow phase of the charging is shown in Figure 6a-III and a-IV and is characterized by slow, diffusion-limited transport of ions from the gap into the electrode. As mentioned earlier, this diffusion-limited ionic transport is a characteristic of fbCDI systems.[26,29] At times $\bar{t}$ = 1 and 2, the electric field at the electrode−gap interface is reduced to, respectively, 1.5% and 1% of its initial value, favoring diffusive interchange of ions over electromigration (see Figure S6a). The angled contour lines within the electrode for times $\bar{t}$ = 4−8 (see video provided in the Supporting Information) subsequently show how this process is limited by the influx of ions entering the cell and then diffusing into the electrode, predominantly entering the electrode at the electrode surfaces nearest the inlet. Note the near vertical portions of the concentration contours at $\bar{t}$ = 8, indicating the importance and persistence of 2D transport in the charging of this system.

Figure 1b shows concentration fields immediately after the cell is short circuited at $\bar{t}$ = 14. The color bar range is here from 1 to 2 to aid in visual representation (the maximum nondimensional concentration in the discharge process is about 3). We see a rapidly formed desorption region in the near-gap region of the electrode. This high-concentration region expands, and its boundary propagates to the top of the electrode. In a manner analogous to the charging process, the

DOI: 10.1021/acs.jpcc.5b05847
J. Phys. Chem. C XXXX, XXX, XXX−XXX

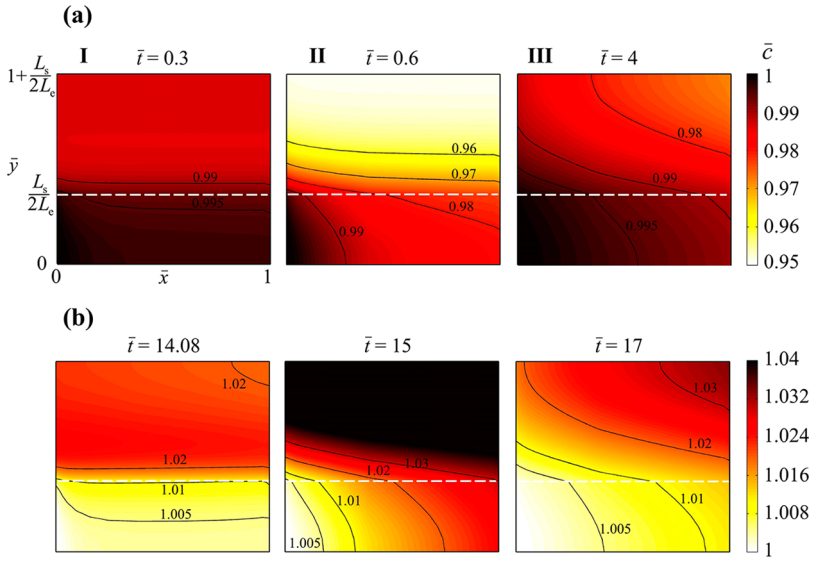

Figure 7. Ion concentration fields in gap and macropores normalized by a 200 mM inlet concentration. Shown is the not to scale top half of the cell for constant voltage (a) charging (1 V) and (b) discharging (0 V). All other parameters are similar to those of Figure 6. In a similar manner to Figure 6, a depletion region rapidly forms inside the electrodes and charging rate is then limited by diffusion. However, the diffusion-limited charging process occurs faster than the 20 mM case. We hypothesize this difference is associated with electrode starvation, which is only observed in the low-concentration (20 mM) case. Discharge process shows an analogous trend, i.e., rapid but brief discharge followed by slow diffusion.

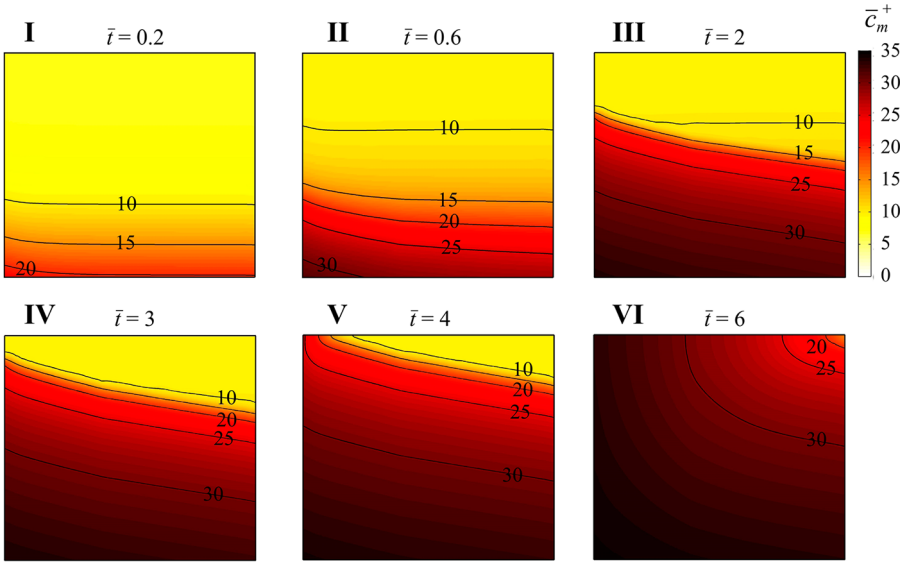

Figure 8. Normalized micropore concentration profiles in the upper electrode for 20 mM inlet concentration during charging. Note that plots are not to scale. Micropores in the regions near the solution−electrode interface (lower edge of squares) are almost completely charged quickly, while the rest of the micropores remain partially charged. As time goes on, the interface between low- and high-concentration regions becomes thinner and propagates toward the collector boundary (upper edge of squares) until all micropores are completely charged.

desorption covers the entire electrode within a period of about $\Delta\bar{t} = 1$. This rapid propagation is then followed by a low-electric field, slow, diffusion-limited transport of ions out of the electrode. See the electric potential in the cell for selected times in Figure S6. In the Supporting Information (Figure S2), we present line plots (along $\bar{x} = 1/2$) associated with the results of Figure 6.

5.2. Macropore Concentration for High Inlet Concentration. We here present additional results for high inlet concentration (200 mM) and compare these to the low-concentration simulations of the previous section. For 200 mM, the salt adsorption capacity is smaller than the salt initially within the total cell volume. The ratio of salt capacity to initial salt in this case is about 0.45. Figure 7 shows the gap and electrode concentration at selected times similar to those of Figure 6. Note that the normalized concentrations through the cell and for the entire charging and discharging processes are now near unity. This is expected from the smaller ratio of adsorption capacity to initial salt. Despite the mild changes in concentration, the simulations show many of the multidimensional transport features discussed in the previous section. These include the fast and slow dynamics as well as the high-angle contours associated with trade offs between advection and diffusion.

In the Supporting Information (Figure S3), we present the line plots associated with Figure 7 along the line $\bar{x} = 1/2$. The

DOI: 10.1021/acs.jpcc.5b05847
J. Phys. Chem. C XXXX, XXX, XXX−XXX

results show that the time scales for the fast adsorption phase of the charging process as well as the discharge process are similar to those of the 20 mM case. For example, the minimum concentration (at the end of fast adsorption phase) occurs at around $\bar{t} = 1$. Also, the time scales associated with the discharge process are similar to those of the low-concentration case. Interestingly, the qualitative shape of normalized concentration curves in discharge is also very similar to that of low-concentration curves (cf. Figures S2b and S3b). However, the results here are different from the low-concentration case in two ways. First, no electrode starvation is observed as the amount of salt initially in the system is less than the total salt capacity of the cell even for 1 V applied potential. Second, the charging process is now significantly faster. For example, the concentration field contour lines at $\bar{t} = 4$ for 200 mM (Figure 7a-III) are similar to $\bar{t} = 8$ for 20 mM (Figure 6a-IV). During starvation (in times between $\bar{t} \approx 1-5$ in 20 mM case), some portion of the electrode has a negligible concentration, and hence, no ion adsorption is possible in those regions. The electrode is then forced to rely only on diffused ions for adsorption. In contrast, for the high-concentration case, the electrode can adsorb due to both locally available supply of ions and diffusion of ions. Hence, charging is eventually dominated by diffusive transport of ions from bulk solution in both low- and high-concentration cases explored here. However, the main difference between these is that in the low-concentration case starvation more strongly retards the charging process. We hypothesize that diffusive transport will have an increasingly negligible effect on charging time as initial salt supply becomes progressively higher than the electrode capacity.

5.3. Micropore Concentration and Evidence of a Concentration Shock. As mentioned above, we characterize the end of the initial rapid phases of charging and discharging (at roughly $\bar{t} = 0-1$ for charging and $\bar{t} = 14-15$ for discharging) as a transition to diffusion-dominated transport. However, we again stress this transition does not necessarily imply fully charged micropores. We demonstrate this effect in Figure 8, where we plot normalized micropore counterion concentration (a measure of micropores charging level) throughout the upper electrode in the charging process for 20 mM inlet salt concentration. We also present line plots associated with Figure 8 along $\bar{x} = 1/2$ in Figure S4 during charging and discharging.

Figure 8 shows that the near-interface micropores (lower edge of squares) are rapidly charged upon application of external voltage, while the rest of the micropores remain partially charged. The ion diffusive transport from bulk solution coupled with local adsorption into the partially charged micropores results in a steepening of the micropore concentration profile within the electrode. As shown in Figure 8, the interplay of diffusive transport and local adsorption continuously sharpens the low- and high-charge state micropores and results in what appears to be a propagating shock wave in ion concentration. This shock wave propagation was observed in the 1D mD model of Porada et al.,[73] although Porada presents no discussion of its physical origin. We here present a hypothesis for formation of such interface. In Figure S5, we show directional diffusion flux $-\partial\bar{c}/\partial\bar{y}$ and local (instantaneous) salt adsorption rate $\partial\bar{w}_m/\partial\bar{t}$ along $\bar{x} = 1/2$ within the electrode. The diffusive flux distribution quickly forms a step-like function, with a rapid drop in flux within the electrode. The step function in flux coincides with a spatial peak in the adsorption rate. This is evidence that the starved micropores are forced to "wait" for diffusion. We refer the reader to section S4 of the Supporting Information for more discussion. A movie of the predicted concentration fields associated with this simulation is also available as the Supporting Information.

We further discuss the results for the high-salt concentration case here. Our simulations for the charging process for 200 mM salt concentration (not presented here) show no concentration shock within the electrodes. For 200 mM concentrations, micropores are almost uniformly charged upon application of voltage. As we mentioned earlier, for 200 mM, the salt initially in the gap and electrodes is abundant, and this implies no starvation. We hypothesize the shock wave is the result of local electrode starvation (where at least some region of the electrode is starved), and this is only observed in the low-concentration case.

In the Supporting Information (section S5) we further discuss the micropore potential distribution and its correlation to micropore charge state. This includes plots of micropore potential along the line $\bar{x} = 1/2$ at selected times during the charging and discharging process.

6. CONCLUSIONS

In this paper, we formulated and solved what is to our knowledge the first 2D model of a CDI cell. This model included coupled solutions of external electrical networks, charge conservation, and species conservation in bimodal pore structure electrodes. We coupled the desalination cell to an arbitrary voltage- or current-control external power source (with a purely resistive element). The model includes three free parameters $\bar{\mu}_{ati}$, C_m, and p_m which, respectively, characterize nonelectrostatic adsorption of ions into micropores, volume-normalized adsorption capacitance of micropores, and porosity of micropores. We applied the model to a flow-between architecture desalination cell (with a water-filled gap between a single pair of porous electrodes). We built a mesoscale fbCDI cell and performed a series of experiments at constant external voltage and constant flow rate in an open loop configuration (i.e., constant inlet species concentrations). We chose a low influent concentration (20 mM) as a test case in our experiments to investigate strong ion removal and study diffusion-limited desalination.

We calibrated the model by using dynamics effluent salt and near-equilibrium salt and charge data. The extracted free parameters are fixed throughout the whole work. We presented effluent salt concentration as well as cumulative and equilibrium adsorbed salt and transferred charge as a function of time. We showed a reasonable agreement between model results and experimental data. The measured effluent concentration suggested that the desalination process in fbCDI cells has two distinct phases: a fast adsorption step at the beginning of charging followed by a slow salt removal step.

We performed numerical simulations to investigate the adsorption/desorption dynamics in a capacitive deionization cell operated under continuous flow rate. We performed simulations at low (20 mM KCl) and high (200 mM KCl) inlet salt concentrations. We presented predictions for the spatiotemporal evolution of potential as well as ion concentrations in the gap, macropores, and micropores. We showed that low inlet concentration can lead to electrode starvation (near zero macropore concentration). The coupling of diffusion-limited transport and adsorption can result in a sharpening of the gradient between high and low micropore

DOI: 10.1021/acs.jpcc.5b05847
J. Phys. Chem. C XXXX, XXX, XXX−XXX

charge concentration. This sharpening apparently results in an ion concentration shock wave in micropore charge concentration propagating through the electrode (toward the current collector). We hypothesize this shock wave is caused by the coupling of diffusion and adsorption in the low-concentration regime where adsorption can lead to local electrode starvation.

■ ASSOCIATED CONTENT

Supporting Information

The Supporting Information is available free of charge on the ACS Publications website at DOI: 10.1021/acs.jpcc.5b05847.

Discussion on effect of electrode compression on contact resistance; figure of three-dimensional drawing of CDI cell clamshell structure; figure of normalized macropore concentration along the line $\bar{x} = 1/2$ for 20 and 200 mM inlet concertation; figure of normalized micropore concentration for 20 mM inlet salt concentration; figure of normalized diffusion flux in the y direction and local salt adsorption rate during the charging process; figure of normalized macropore potential (PDF)

Videos of the micropore and macropore spatiotemporal concentration field in the upper-half of the system during charging and discharging processes (ZIP)

■ AUTHOR INFORMATION

Corresponding Author

*Phone: 650-736-1283. Fax: 650-723-7657. E-mail: juan.santiago@stanford.edu.

Notes

The authors declare no competing financial interest.

■ ACKNOWLEDGMENTS

This work was supported by LLNL LDRD project 15-ERD-068. Work at LLNL was performed under the auspices of the US DOE by LLNL under Contract DE-AC52-07NA27344. A.H. gratefully acknowledges the support from Krishna Kolluri Engineering Graduate Fellowship as well as the Stanford Graduate Fellowship program.

■ REFERENCES

(1) De Levie, R. On Porous Electrodes in Electrolyte Solutions: I. Capacitance Effects. *Electrochim. Acta* **1963**, *8*, 751−780.

(2) De Levie, R. On Porous Electrodes in Electrolyte solutions—IV. *Electrochim. Acta* **1964**, *9*, 1231−1245.

(3) Murphy, G. W.; Caudle, D. D. Mathematical Theory of Electrochemical Demineralization in Flowing Systems. *Electrochim. Acta* **1967**, *12* (12), 1655−1664.

(4) Oren, Y.; Soffer, a. Water Desalting by Means of Electrochemical Parametric Pumping - I. The Equilibrium Properties of a Batch Unit Cell. *J. Appl. Electrochem.* **1983**, *13* (4), 473−487.

(5) Johnson, A. M.; Newman, J. Desalting by Means of Porous Carbon Electrodes. *J. Electrochem. Soc.* **1971**, *118* (3), 510.

(6) Newman, J.; Tiedemann, W. Porous-Electrode Theory with Battery Applications. *AIChE J.* **1975**, *21*, 25−41.

(7) Newman, J.; Thomas-Alyea, K. E. *Electrochemical Systems*; John Wiley & Sons: New York, 2012.

(8) Biesheuvel, P. M.; Bazant, M. Z. Nonlinear Dynamics of Capacitive Charging and Desalination by Porous Electrodes. *Phys. Rev. E* **2010**, *81* (3), 031502.

(9) Suss, M.; Porada, S.; Sun, X.; Biesheuvel, M.; Yoon, J.; Presser, V. Water Desalination via Capacitive Deionization: What Is It and What Can We Expect from It? *Energy Environ. Sci.* **2015**, *8*, 2296.

(10) Demirer, O. N.; Naylor, R. M.; Rios Perez, C. A.; Wilkes, E.; Hidrovo, C. Energetic Performance Optimization of a Capacitive Deionization System Operating with Transient Cycles and Brackish Water. *Desalination* **2013**, *314*, 130−138.

(11) Demirer, O. N.; Clifton, R. L.; Rios Perez, C. A.; Naylor, R.; Hidrovo, C. Characterization of Ion Transport and -Sorption in a Carbon Based Porous Electrode for Desalination Purposes. *J. Fluids Eng.* **2013**, *135* (4), 041201.

(12) Rios Perez, C. A.; Demirer, O. N.; Clifton, R. L.; Naylor, R. M.; Hidrovo, C. H. Macro Analysis of the Electro-Adsorption Process in Low Concentration NaCl Solutions for Water Desalination Applications. *J. Electrochem. Soc.* **2013**, *160* (3), E13−E21.

(13) Zhao, R.; Satpradit, O.; Rijnaarts, H. H. M.; Biesheuvel, P. M.; van der Wal, A. Optimization of Salt Adsorption Rate in Membrane Capacitive Deionization. *Water Res.* **2013**, *47* (5), 1941−1952.

(14) Biesheuvel, P.; Suss, M.; Hamelers, H. V. M Theory of Water Desalination by Porous Electrodes with Fixed Chemical Charge. *arXiv preprint arXiv:1506.03948*; 2015.

(15) Mirzadeh, M.; Gibou, F.; Squires, T. M. Enhanced Charging Kinetics of Porous Electrodes: Surface Conduction as a Short-Circuit Mechanism. *Phys. Rev. Lett.* **2014**, *113* (9), 097701.

(16) Gabitto, J.; Tsouris, C. Volume Averaging Study of the Capacitive Deionization Process in Homogeneous Porous Media. *Transp. Porous Media* **2015**, *109* (1), 61−80.

(17) Rica, R. a.; Ziano, R.; Salerno, D.; Mantegazza, F.; Bazant, M. Z.; Brogioli, D. Electro-Diffusion of Ions in Porous Electrodes for Capacitive Extraction of Renewable Energy from Salinity Differences. *Electrochim. Acta* **2013**, *92*, 304−314.

(18) Yuan, L.; Yang, X.; Liang, P.; Wang, L.; Huang, Z. H.; Wei, J.; Huang, X. Capacitive Deionization Coupled with Microbial Fuel Cells to Desalinate Low-Concentration Salt Water. *Bioresour. Technol.* **2012**, *110*, 735−738.

(19) Deeke, A.; Sleutels, T. H. J. A.; Hamelers, H. V. M; Buisman, C. J. N. Capacitive Bioanodes Enable Renewable Energy Storage in Microbial Fuel Cells. *Environ. Sci. Technol.* **2012**, *46* (6), 3554−3560.

(20) Simon, P.; Gogotsi, Y. Materials for Electrochemical Capacitors. *Nat. Mater.* **2008**, *7* (11), 845−854.

(21) Stoller, M. D.; Ruoff, R. S. Best Practice Methods for Determining an Electrode Material's Performance for Ultracapacitors. *Energy Environ. Sci.* **2010**, *3*, 1294.

(22) Dunn, D.; Newman, J. Predictions of Specific Energies and Specific Powers of Double-Layer Capacitors Using a Simplified Model. *J. Electrochem. Soc.* **2000**, *147*, 820.

(23) Bijmans, M. F. M.; Burheim, O. S.; Bryjak, M.; Delgado, A.; Hack, P.; Mantegazza, F.; Tenisson, S.; Hamelers, H. V. M CAPMIX - Deploying Capacitors for Salt Gradient Power Extraction. *Energy Procedia* **2012**, *20*, 108−115.

(24) Liu, F.; Wagterveld, R. M.; Gebben, B.; Otto, M. J.; Biesheuvel, P. M.; Hamelers, H. V. M Carbon Nanotube Yarns as Strong Flexible Conductive Capacitive Electrodes. *Colloids Interface Sci. Commun.* **2014**, *3* (2014), 9−12.

(25) Porada, S.; Weingarth, D.; Hamelers, H. V. M; Bryjak, M.; Presser, V.; Biesheuvel, P. M. Carbon Flow Electrodes for Continuous Operation of Capacitive Deionization and Capacitive Mixing Energy Generation. *J. Mater. Chem. A* **2014**, *2* (24), 9313.

(26) Suss, M. E.; Baumann, T. F.; Bourcier, W. L.; Spadaccini, C. M.; Rose, K. a.; Santiago, J. G.; Stadermann, M. Capacitive Desalination with Flow-through Electrodes. *Energy Environ. Sci.* **2012**, *5* (11), 9511.

(27) Oren, Y. Capacitive Deionization (CDI) for Desalination and Water Treatment — Past, Present and Future (a Review). *Desalination* **2008**, *228* (1−3), 10−29.

(28) Jeon, S. I.; Park, H. R.; Yeo, J. G.; Yang, S.; Cho, C. H.; Han, M. H.; Kim, D. K. Desalination via a New Membrane Capacitive Deionization Process Utilizing Flow-Electrodes. *Energy Environ. Sci.* **2013**, *6* (5), 1471−1475.

(29) Suss, M. E.; Biesheuvel, P. M.; Baumann, T. F.; Stadermann, M.; Santiago, J. G. In Situ Spatially and Temporally Resolved Measurements of Salt Concentration between Charging Porous Electrodes for

DOI: 10.1021/acs.jpcc.5b05847
J. Phys. Chem. C XXXX, XXX, XXX−XXX

Desalination by Capacitive Deionization. *Environ. Sci. Technol.* **2014**, *48* (3), 2008−2015.
(30) Bouhadana, Y.; Avraham, E.; Soffer, A.; Aurbach, D. Several Basic and Practical Aspects Related to Electrochemical Deionization of Water. *AIChE J.* **2009**, *56* (3), 779−789.
(31) Biesheuvel, P. M.; van Limpt, B.; van der Wal, A. Dynamic Adsorption/Desorption Process Model for Capacitive Deionization. *J. Phys. Chem. C* **2009**, *113* (14), 5636−5640.
(32) Biesheuvel, P. M.; Fu, Y.; Bazant, M. Z. Diffuse Charge and Faradaic Reactions in Porous Electrodes. *Phys. Rev. E* **2011**, *83* (6), 061507.
(33) Biesheuvel, P. M.; Zhao, R.; Porada, S.; van der Wal, A. Theory of Membrane Capacitive Deionization Including the Effect of the Electrode Pore Space. *J. Colloid Interface Sci.* **2011**, *360* (1), 239−248.
(34) Porada, S.; Borchardt, L.; Oschatz, M.; Bryjak, M.; Atchison, J. S.; Keesman, K. J.; Kaskel, S.; Biesheuvel, P. M.; Presser, V. Direct Prediction of the Desalination Performance of Porous Carbon Electrodes for Capacitive Deionization. *Energy Environ. Sci.* **2013**, *6* (12), 3700.
(35) Biesheuvel, P. M.; Fu, Y.; Bazant, M. Z. Electrochemistry and Capacitive Charging of Porous Electrodes in Asymmetric Multicomponent Electrolytes. *Russ. J. Electrochem.* **2012**, *48* (6), 580−592.
(36) Stern, O. The Theory of the Electrolytic Double-Layer. *Z. Elektrochem.* **1924**, *30*, 508−516.
(37) Wang, H.; Pilon, L. Accurate Simulations of Electric Double Layer Capacitance of Ultramicroelectrodes. *J. Phys. Chem. C* **2011**, *115* (33), 16711−16719.
(38) Kastening, B.; Heins, M. Properties of Electrolytes in the Micropores of Activated Carbon. *Electrochim. Acta* **2005**, *50* (12), 2487−2498.
(39) Corapcioglu, M. O.; Huang, C. P. The Adsorption of Heavy Metals onto Hydrous Activated Carbon. *Water Res.* **1987**, *21* (9), 1031−1044.
(40) Chuang, C. L.; Fan, M.; Xu, M.; Brown, R. C.; Sung, S.; Saha, B.; Huang, C. P. Adsorption of arsenic(V) by Activated Carbon Prepared from Oat Hulls. *Chemosphere* **2005**, *61* (4), 478−483.
(41) Hunter, R. J. *Zeta Potential in Colloid Science: Principles and Applications*; Academic Press: New York, 2013.
(42) Levi, M. D.; Sigalov, S.; Salitra, G.; Elazari, R.; Aurbach, D. Assessing the Solvation Numbers of Electrolytic Ions Confined in Carbon Nanopores under Dynamic Charging Conditions. *J. Phys. Chem. Lett.* **2011**, *2*, 120−124.
(43) Biesheuvel, P. M.; Porada, S.; Levi, M.; Bazant, M. Z. Attractive Forces in Microporous Carbon Electrodes for Capacitive Deionization. *J. Solid State Electrochem.* **2014**, *18* (5), 1365−1376.
(44) Gerischer, H. An Interpretation of the Double Layer Capacity of Graphite Electrodes in Relation to the Density of States at the Fermi Level. *J. Phys. Chem.* **1985**, *89* (20), 4249−4251.
(45) Gerischer, H.; McIntyre, R.; Scherson, D.; Storck, W. Density of the Electronic States of Graphite: Derivation from Differential Capacitance Measurements. *J. Phys. Chem.* **1987**, *91* (7), 1930−1935.
(46) Porada, S.; Weinstein, L.; Dash, R.; van der Wal, A.; Bryjak, M.; Gogotsi, Y.; Biesheuvel, P. M. Water Desalination Using Capacitive Deionization with Microporous Carbon Electrodes. *ACS Appl. Mater. Interfaces* **2012**, *4* (3), 1194−1199.
(47) Qu, Y.; Baumann, T. F.; Santiago, J. G.; Stadermann, M. Characterization of Resistances of a Capacitive Deionization System. *Environ. Sci. Technol.* **2015**, *49* (16), 9699−9706.
(48) Mezedur, M. M.; Kaviany, M.; Moore, W. Effect of Pore Structure, Randomness and Size on Effective Mass Diffusivity. *AIChE J.* **2002**, *48* (1), 15−24.
(49) Weissberg, H. L. Effective Diffusion Coefficient in Porous Media. *J. Appl. Phys.* **1963**, *34* (1963), 2636−2639.
(50) Van Brakel, J.; Heertjes, P. M. Analysis of Diffusion in Macroporous Media in Terms of a Porosity, a Tortuosity and a Constrictivity Factor. *Int. J. Heat Mass Transfer* **1974**, *17*, 1093−1103.
(51) Mu, D.; Liu, Z.-S.; Huang, C.; Djilali, N. Determination of the Effective Diffusion Coefficient in Porous Media Including Knudsen Effects. *Microfluid. Nanofluid.* **2008**, *4* (3), 257−260.
(52) Das, P. K.; Li, X.; Liu, Z. S. Effective Transport Coefficients in PEM Fuel Cell Catalyst and Gas Diffusion Layers: Beyond Bruggeman Approximation. *Appl. Energy* **2010**, *87* (9), 2785−2796.
(53) Hirokawa, T.; Nishino, M.; Aoki, N.; Kiso, Y.; Sawamoto, Y.; Yagi, T.; Akiyama, J.-I. Table of Isotachophoretic Indices: I. Simulated Qualitative and Quantitative Indices of 287 Anionic Substances in the Range Ph 3−10. *J. Chromatogr. A* **1983**, *271*, D1−D106.
(54) Hirokawa, T.; Gojo, T.; Kiso, Y. Isotachophoretic Determination of Mobility and pKa by Means of Computer Simulation. IV. Evaluation of m0 and pKa of Twenty-Six Amino Acids and Assessment of the Separability. *J. Chromatogr.* **1986**, *369*, 59−81.
(55) Biesheuvel, P. M.; van der Wal, A. Membrane Capacitive Deionization. *J. Membr. Sci.* **2010**, *346* (2), 256−262.
(56) Brogioli, D.; Zhao, R.; Biesheuvel, P. M. A Prototype Cell for Extracting Energy from a Water Salinity Difference by Means of Double Layer Expansion in Nanoporous Carbon Electrodes. *Energy Environ. Sci.* **2011**, *4* (3), 772.
(57) Choi, J.-H. Determination of the Electrode Potential Causing Faradaic Reactions in Membrane Capacitive Deionization. *Desalination* **2014**, *347*, 224−229.
(58) Cohen, I.; Avraham, E.; Bouhadana, Y.; Soffer, A.; Aurbach, D. The Effect of the Flow-Regime, Reversal of Polarization, and Oxygen on the Long Term Stability in Capacitive de-Ionization Processes. *Electrochim. Acta* **2015**, *153*, 106−114.
(59) Jande, Y. a. C.; Kim, W. S. Modeling the Capacitive Deionization Batch Mode Operation for Desalination. *J. Ind. Eng. Chem.* **2014**, *20*, 3356.
(60) Kang, J.; Kim, T.; Jo, K.; Yoon, J. Comparison of Salt Adsorption Capacity and Energy Consumption between Constant Current and Constant Voltage Operation in Capacitive Deionization. *Desalination* **2014**, *352*, 52−57.
(61) Długołęcki, P.; van der Wal, A. Energy Recovery in Membrane Capacitive Deionization. *Environ. Sci. Technol.* **2013**, *47* (9), 4904−4910.
(62) Kim, T.; Dykstra, J. E.; Porada, S.; van der Wal, A.; Yoon, J.; Biesheuvel, P. M. Enhanced Charge Efficiency and Reduced Energy Use in Capacitive Deionization by Increasing the Discharge Voltage. *J. Colloid Interface Sci.* **2015**, *446*, 317.
(63) Bouhadana, Y.; Ben-Tzion, M.; Soffer, A.; Aurbach, D. A Control System for Operating and Investigating Reactors: The Demonstration of Parasitic Reactions in the Water Desalination by Capacitive de-Ionization. *Desalination* **2011**, *268* (1−3), 253−261.
(64) Zhao, R.; Biesheuvel, P. M.; van der Wal, A. Energy Consumption and Constant Current Operation in Membrane Capacitive Deionization. *Energy Environ. Sci.* **2012**, *5* (11), 9520.
(65) Zhao, R.; Biesheuvel, P. M.; Miedema, H.; Bruning, H.; van der Wal, A. Charge Efficiency: A Functional Tool to Probe the Double-Layer Structure Inside of Porous Electrodes and Application in the Modeling of Capacitive Deionization. *J. Phys. Chem. Lett.* **2010**, *1* (1), 205−210.
(66) Biesheuvel, P. M. Thermodynamic Cycle Analysis for Capacitive Deionization. *J. Colloid Interface Sci.* **2009**, *332* (1), 258−264.
(67) Suss, M. E.; Baumann, T. F.; Worsley, M. a.; Rose, K. a.; Jaramillo, T. F.; Stadermann, M.; Santiago, J. G. Impedance-Based Study of Capacitive Porous Carbon Electrodes with Hierarchical and Bimodal Porosity. *J. Power Sources* **2013**, *241*, 266−273.
(68) Yoon, S.; Jang, J. H.; Ka, B. H.; Oh, S. M. Complex Capacitance Analysis on Rate Capability of Electric-Double Layer Capacitor (EDLC) Electrodes of Different Thickness. *Electrochim. Acta* **2005**, *50* (11), 2255−2262.
(69) Eikerling, M.; Kornyshev, a. a.; Lust, E. Optimized Structure of Nanoporous Carbon-Based Double-Layer Capacitors. *J. Electrochem. Soc.* **2005**, *152* (1), E24.
(70) Pell, W. G.; Conway, B. E.; Marincic, N. Analysis of Non-Uniform Charge/discharge and Rate Effects in Porous Carbon Capacitors Containing Sub-Optimal Electrolyte Concentrations. *J. Electroanal. Chem.* **2000**, *491* (1−2), 9−21.

DOI: 10.1021/acs.jpcc.5b05847
J. Phys. Chem. C XXXX, XXX, XXX−XXX

(71) Pell, W. G.; Conway, B. E. Analysis of Power Limitations at Porous Supercapacitor Electrodes under Cyclic Voltammetry Modulation and Dc Charge. *J. Power Sources* **2001**, *96*, 57−67.
(72) Mysyk, R.; Raymundo-Piñero, E.; Béguin, F. Saturation of Subnanometer Pores in an Electric Double-Layer Capacitor. *Electrochem. Commun.* **2009**, *11* (3), 554−556.
(73) Porada, S.; Zhao, R.; van der Wal, A.; Presser, V.; Biesheuvel, P. M. Review on the Science and Technology of Water Desalination by Capacitive Deionization. *Prog. Mater. Sci.* **2013**, *58* (8), 1388−1442.

DOI: 10.1021/acs.jpcc.5b05847
J. Phys. Chem. C XXXX, XXX, XXX−XXX